

Green, HF-Free Synthesis of MXene Quantum Dots and their Photocatalytic Activity for Hydrogen Evolution

Rubén Ramírez, Arianna Melillo, Silvio Osella, Abdullah M. Asiri, Hermenegildo Garcia,* and Ana Primo*

A general methodology to prepare MXene quantum dots (MxQDs) with yields over 20% by liquid-phase laser ablation of the MAX phase is reported. Mechanical and thermal shock by 532 nm laser pulses (7 ns fwhp, 50 mJ) × pulse⁻¹, 1 Hz pulse frequency) produces MAX etching and exfoliation to form MXene QDs, avoiding the use of HF. The process can be followed by absorption and emission spectroscopy and by dynamic laser scattering and it appears to be general, being applied to Ti₃AlC₂, Ti₂AlC, Nb₂AlC, and V₂AlC MAX phases. Density functional theory calculations indicate that, depending on the surface terminal groups, the diminution of the MXene size to the nanometric scale makes it possible to control the band gap of the MXene. The photocatalytic activity of these MXene QDs for hydrogen evolution has been observed, reaching an H₂ production for the most efficient Ti₃C₂ QDs as high as 2.02 mmol × g⁻¹ × h⁻¹.

layer (X), the latter always internal and sandwiched between two metal sheets.^[1–3] MXenes can be obtained by etching of the A element and delamination of the corresponding MAX phase by the removal of Al³⁺ with HF.^[2,4–7] Due to the corrosive and hazardous risks associated with the use of concentrated aqueous HF solutions, there is a need to develop alternative green delamination procedures.

The properties of the MXenes depend on a number of compositional and structural parameters, including the nature of the M and X elements, the nature of the surface terminal groups, and the number of atom layers among others.^[7–12] To enlarge the range of applications of MXenes, it would be convenient to apply

the versatility offered by MXenes to tune their optoelectronic properties.^[13–16] In particular, for application in photocatalysis, it is necessary to control the band gap of these materials and to align the energy of the conduction and valence bands to the optimal potentials to promote a particular chemical reaction.^[15,17–20]

Considering the two commented problems of MXene synthesis, that is, the use of concentrated HF solutions to etch the MAX phase and the control of the semiconducting properties of MXenes, it occurred to us that innovative preparation procedures could be used to avoid HF while transforming a conductive MXene into a semiconductor material for its use in photocatalysis.^[21] Herein it is reported that laser ablation of the MAX phases is a general procedure to prepare MXene quantum dots (MxQDs) that are able to evolve hydrogen photocatalytically upon irradiation with Vis light.

Quantum dots (QDs) are particles below 10 nm that exhibit remarkable properties due to the confinement of electrons in a small volume of nanometric dimension.^[22–33] We reported that laser ablation of graphitic carbons in aqueous suspension is a general way to produce graphene QDs.^[31] The energy of a Nd-YAG pulsed laser beam focused on a small area of nanometric dimension delivered in a short nanosecond pulse provides high power on a small volume of the particle. This energy in a short time is able to cause sufficient mechanical and thermal stress, producing delamination of the loosely-packed graphene sheets of the graphitic carbon. Other layered materials, such as MoS₂, also form 2D quantum dots upon laser ablation of the bulk crystals.^[34] It occurred to us that similar laser ablation with pulsed laser beams could also produce the unprecedented formation of


1. Introduction

MXenes are 2D materials of a few atoms' thicknesses constituted by alternate layers of a metal (M) and a carbon or carbon-nitride

R. Ramírez, A. Melillo, H. Garcia, A. Primo
Instituto Universitario de Tecnología Química
Universitat Politècnica de Valencia-Consejo Superior de Investigaciones Científicas
Valencia 46022, Spain
E-mail: hgarcia@qim.upv.es; aprimoar@qim.upv.es

S. Osella
Chemical and Biological Systems Simulation Lab
Centre of New Technologies
University of Warsaw
Warsaw 02–097, Poland
S. Osella
Materials and Process Simulation Center (mc 134–74)
California Institute of Technology
Pasadena, CA 91125, USA

A. M. Asiri, H. Garcia
Center of Excellence for Advanced Materials
King Abdulaziz University
Jeddah 21589, Saudi Arabia

 The ORCID identification number(s) for the author(s) of this article can be found under <https://doi.org/10.1002/smt.202300063>

© 2023 The Authors. Small Methods published by Wiley-VCH GmbH. This is an open access article under the terms of the Creative Commons Attribution-NonCommercial License, which permits use, distribution and reproduction in any medium, provided the original work is properly cited and is not used for commercial purposes.

DOI: 10.1002/smt.202300063

MXene QDs (MxQDs), although, in the case of graphite and bulk MoS₂, the interaction between the layers by van der Waals forces are much weaker than the reticular bonds of MAX phases.

The formation of MxQDs has been recently reported.^[35] However, the properties of these novel materials, except perhaps photoluminescence,^[35] remain essentially unexplored as well as general methods in which these MxQDs can be formed.^[35,36] The first reference in the bibliography about MxQDs was probably in 2017 by Zhi et al. who synthesized for cellular imaging photoluminescent Ti₃C₂ QDs prepared after etching the corresponding MAX phase with concentrated aqueous HF, followed by hydrothermal treatment to diminish the particle size.^[35] In the same year, another publication by Liu et al. synthesized F-free MxQDs from the MAX phase by strong ultrasonication, followed by treatment with corrosive tetrabutylammonium hydroxide as Al³⁺ etching agent.^[37] Most of the subsequent reports on MxQDs still use hazardous HF as an exfoliating agent, followed by an additional treatment under hydrothermal conditions or sonication.^[38] Until now, MxQDs have been mostly employed in biomedical applications, due to their emission properties, resulting in multicolored cellular imaging.^[35,36,39–41]

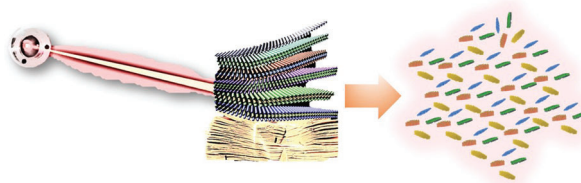
Herein it is reported that ns pulses of Nd-YAG laser produce ablation of various MAX phases resulting in the generation of MxQDs. The method reported here presents several advantages with respect to the current state of the art. On one hand, the process avoids the use of noxious concentrated HF and leads to the presence of surface oxygenated terminal groups. On the other hand, the method is applied to the MAX phase, resulting in the direct formation of the corresponding MxQDs from MAX in a single step. The method is environmentally friendly, does not require any chemical reagent, and appears to be general for the four MAX phases tested. In comparison, a recent precedent used MXene targets as precursors of MxQDs formed by femtosecond laser irradiation, but these MXenes were obtained by conventional exfoliation using a strongly corrosive mixture of LiF in 9 M HCl solution.^[42] The laser beam was used just to break MXene sheets into smaller pieces.^[42] Exfoliation of the MAX phase avoiding the use of HF, as it is reported herein, still remained to be achieved.

Due to the small dimensions, MxQDs should exhibit semiconducting properties.^[43,44] However, the photocatalytic activity of these MxQDs remains unexplored. Herein, we report data on the activity of a series of MxQDs for photocatalytic hydrogen generation. Given the large variety of compositions and the possibility to have a certain control on the average lateral QD size, the present result opens research to find the most efficient MxQD as a photocatalyst for solar fuels production.

2. Results and Discussion

2.1. Preparation of Ti₃C₂ QDs

Scheme 1 illustrates the procedure followed to prepare MxQDs from the corresponding MAX phases. Briefly, the method is based on the 532 nm laser pulse irradiation (7 ns fwhp, 50 mJ × pulse⁻¹, 1 Hz pulse frequency) of the corresponding MAX phase suspended in aqueous solution within a fluorescence quartz cuvette (4 mL) under inert atmosphere. The high power of the laser pulse hitting the MAX nanoparticles should provoke enough mechanical/thermal shock to produce particle damage that would



Scheme 1. MxQDs preparation procedure by laser ablation in liquid phase from the corresponding MAX phases in the absence of any chemical.

lead to the formation of MxQDs as debris. Due to the short duration of the laser pulse (7 ns), its high energy, and the small area, the laser energy could probably destroy the MAX particles through an explosive mass ejection mechanism as proposed in other cases.^[45] As indicated in the introduction, an analogous laser ablation process has been successful for the formation of small particles of chemical elements and other solids,^[23] including graphene quantum dots from graphitic carbon particles^[14c] and MoS₂ quantum dots from bulk MoS₂ crystals.^[15] It was anticipated that the same process could take place from the MAX phase affording MxQDs.

Initial studies were performed using Ti₃AlC₂ MAX solid as a precursor in pure water suspension. The course of Ti₃C₂ QDs evolution was followed by optical absorption spectroscopy monitoring periodically the UV–vis spectrum of the suspension after sedimentation of the large particles, whereby the growth of the baseline with higher absorption in the UV part of the spectrum was observed. Similar continuous absorption with growing absorptivity towards the UV has been recorded for graphene QDs and other carbon-based QDs. Although it will be commented in larger detail later when discussing the photophysical properties, the growth of photoluminescence intensity upon excitation at 350 nm also revealed the increased concentration of QDs. As indicated in Section 1, photoluminescence is a hallmark characteristic of QDs in general and MxQDs in particular and photoluminescence intensity growth can be used to follow the increase in the Ti₃C₂ QD concentration in the suspension upon prolonged laser irradiation. Representative absorption spectra and photoluminescence growth are presented in **Figure 1**.

Dynamic laser scattering (DLS) is a routine technique to monitor and determine the size distribution of particles in suspensions.^[24] DLS also detected the generation of particles in the suspension upon laser treatment with a distribution of particles with defined particle sizes, the largest particles having about 150 nm and the smallest of only a few nm. The particle size was changed during the treatment. In general, the concentration in the aqueous suspension of the smallest particles increases with the time of the laser ablation, suggesting that suspended particles of larger size undergo a subsequent transformation during the process, as observed in the case of Au nanoparticles.^[25] At long irradiation times, DLS measurements reveal that the suspension contains particles of only a few particle sizes. It is proposed that the size distribution and the fact of having a defined particle size are related to the laser beam dimension and its spatial energy distribution.^[23a] **Figure 1** presents representative DLS data on the nanoparticles appearing in the laser ablation and on the zeta potential of the colloidal system.

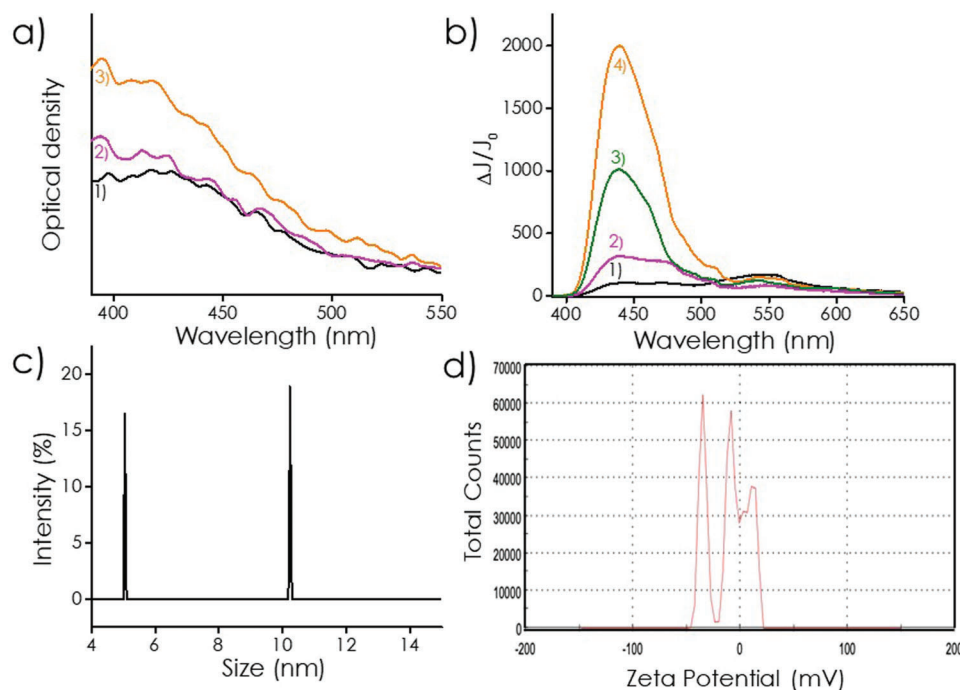


Figure 1. a) UV-vis spectra of Ti_3AlC_2 suspensions after 1) 10, 2) 30, and 3) 90 min laser ablation; b) Emission spectra ($\lambda_{\text{exc}} = 350$ nm) of Ti_3AlC_2 suspensions recorded at 1) 10, 2) 15, 3) 30, and 4) 90 min laser ablation. Size distribution of Ti_3C_2 nanoparticles measured by c) dynamic laser scattering and corresponding d) Z potential from the supernatant after 90 min laser ablation treatment. Reaction conditions: 3 mg of $\text{Ti}_3\text{C}_2\text{Al}$ suspended in a septum-capped 1×1 cm² fluorescence quartz cuvette containing 4 mL of MilliQ water. The suspension was purged with Ar ($1 \text{ mL} \times \text{min}^{-1}$) at least 15 min prior to irradiation. Laser ablation was performed with the second harmonic of an Nd YAG ($50 \text{ m} \times \text{pulse}^{-1}$).

After 2 h irradiation of the suspended MAX phase with 532 nm laser pulses at 1 Hz, the solids were decanted and the resulting suspension was submitted to a two-step centrifugation process, first at 4000 rpm for 4 h and then at 13 000 rpm for 1 h, to remove suspended micrometric particles. After centrifugation, only the smallest nanometric particles remain in the aqueous supernatant dispersion. Estimation by weighing the suspended MxQDs in the final supernatant after exhaustive centrifugation gave a mass of 0.7 mg after 2 h laser treatment starting from 3 mg of MAX phase, corresponding to over 23 wt % of yield. Under our operation conditions, longer reaction times than the optimal (2 h) do not increase the yield of MxQDs, probably due to laser scattering and screening of the formed MxQDs to the remaining MAX particles.

Control experiments in the absence of any MAX phase, submitting to an analogous laser irradiation pure water, did not result in changes in the UV-vis spectra, detection of photoluminescence, or observation of particles by DLS. Although the previously commented studies were carried out in pure water, similar experiments were carried out also in other liquids, such as DMF, observing the same general behavior and the evolution of Ti_3C_2 QDs upon laser ablation of the MAX phase. This could open the door for simultaneous surface functionalization with a variety of terminal groups depending on the solvent used.

Besides indirect evidence of the presence of Ti_3C_2 QD by photoluminescence and DLS, the morphology and particle size of the nanoparticles present in the supernatant after two-step high-speed centrifugation were visualized by high-resolution transmission electron microscopy (HR-TEM) and by atomic force microscopy (AFM). Deposition of a microdrop of the supernatant

on a holey carbon-coated copper sample holder allowed observing by TEM the presence of nanometric QDs in the supernatant with size dispersion between 1 and 20 nm and an average of about 5 nm. **Figure 2** shows some representative images taken from the supernatant after extended laser ablation of MAX and subsequent centrifugation. HR-TEM images at the highest resolution showed that they are crystalline nanoparticles with fringes of 0.261 nm corresponding to the expected lattice value for 110 plane of Ti_3C_2 MXene,^[26] except that, in contrast to previous studies, the lateral size average in the present Ti_3C_2 sample is only of a few nm. Selected area electron diffraction (SAED) of these nanoparticles also indicates that they are crystalline, as deduced from the observation of well-defined bright spots in the diffractograms of the nanoparticles at the nm length scale.

AFM is a very important technique regarding the characterization of 2D materials since it can provide the thickness of nanoparticles.^[27] Although due to the probing tip diameter, the lateral size of nanoparticles cannot be measured with accuracy, AFM gives a very accurate measurement in the vertical scale with subnanometric resolution, when the sample is deposited on an atomically flat surface such as mica, silicon, graphite, and others. For determination of the MxQDs lateral size distribution, dynamic laser scattering in suspension (Figure 1c) or TEM in dry samples (Figure 2a) are the appropriate techniques. AFM images of the supernatant after centrifugation with the procedure indicated earlier of the suspension resulting from $\text{Ti}_3\text{C}_2\text{Al}$ irradiation were in agreement with the information provided by HR-TEM, indicating that the clear supernatant formed after laser ablation contains a multitude of nanoparticles of apparent lateral size up

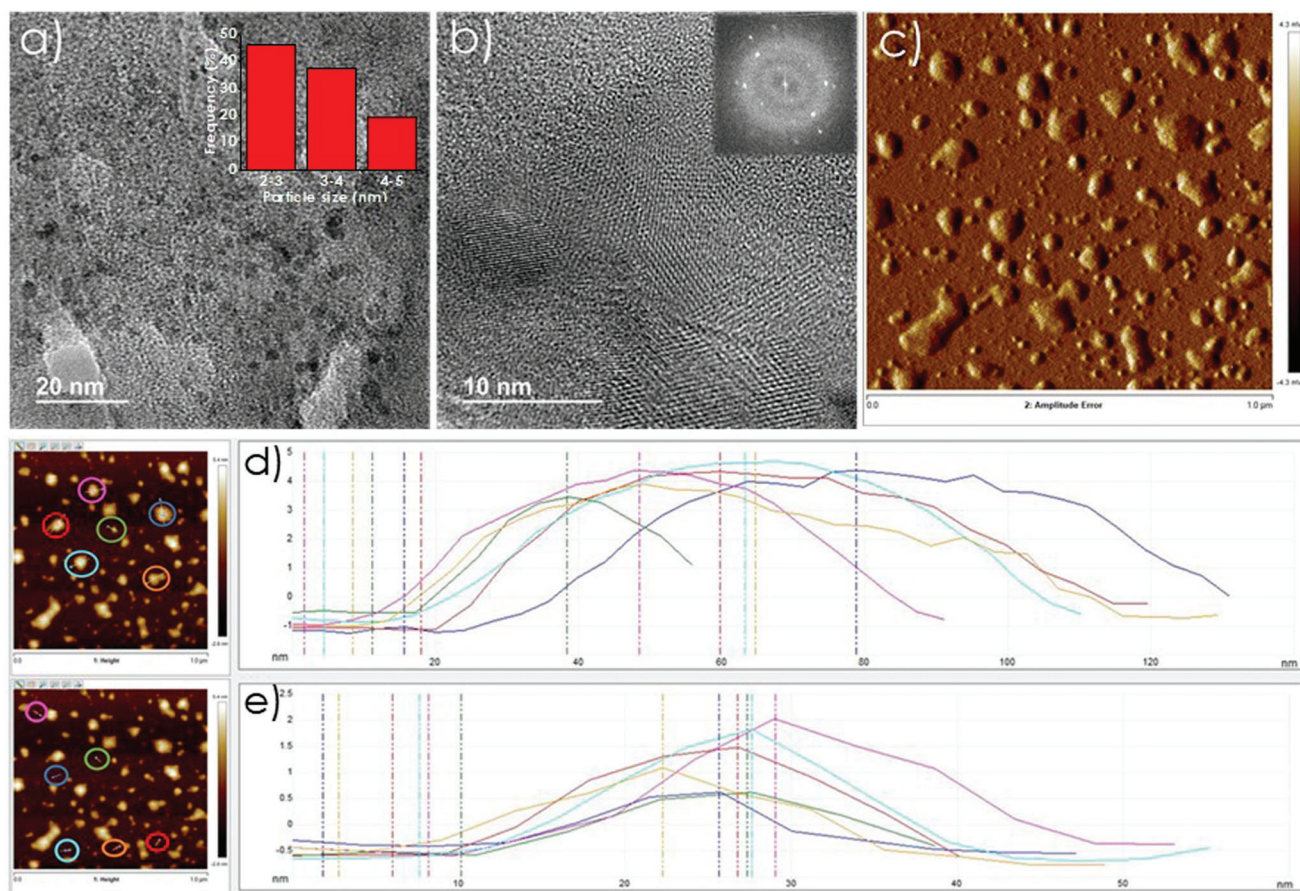


Figure 2. a,b) HR TEM of Ti_3C_2 MXenes formed by laser ablation. Statistical MxQDs particle size gives an average dimension of 5 nm; c) Frontal AFM image of Ti_3C_2 MxQDs and AFM thickness profiles of those nanoparticles circled in different colors in the most left frame corresponding to Ti_3C_2 d) thicker and e) thinner nanoparticles.

to 50 nm and dispersion between 50 and less than 10 nm. Figure 2 presents some frontal views of the Ti_3C_2 QDs formed in the process. Importantly, although the lateral size measurements are not accurate due to the tip size, the thickness of a series of more than 50 nanoparticles showed that they have a narrow height distribution between 1.5 and 4 nm. Figure 2 shows the thickness profile of about ten of these Ti_3C_2 QD nanoparticles showing the narrow thickness distribution of the nanoparticles derived from the laser ablation. The estimated thickness of the Ti_3C_2 monolayer was reported to be 0.95^[28] or 1.5^[29] nm and, therefore most of the nanoparticles formed in the laser ablation process performed here correspond to stacks of 2 to 4 Ti_3C_2 layers, although observation of Ti_3C_2 monolayers of about 1 nm thickness in the laser ablated dispersion was frequent as seen in Figure 2.

Survey XPS spectra revealed the presence of Ti, C, and O, as well as some minor, residual Al in the solid sample after drying the Ti_3C_2 QDs present in the suspension (see Figure S7, Supporting Information). Analysis of the high-resolution XPS peaks of Ti_3C_2 agrees with the presence of Ti–OH and peripheral Ti and C in agreement with the small particle size of MxQDs. Thus, the corresponding Ti 2p of Ti_3C_2 shows a doublet at 455.7 and 461.4 eV attributable, respectively, to the Ti 2p_{3/2} and 2p_{1/2} with four individual components at 459.3, 456.8, 456.0, and 455.4 eV

that can be assigned to Ti atoms C–Ti–OH, C–Ti=O, C–Ti-defects, and C–Ti at the periphery.^[30] The high-resolution XPS C 1s peak was deconvoluted into three components appearing at 282.3, 283.9, and 285.7 eV that agree with C atoms in C–Ti–O coordination, graphitic C (9 at.%) and peripheral C=O (12 at.%), respectively. XPS O1s peak exhibits four components at 531.2, 530.0, 529.3, and 527.9 eV that can be ascribed to O atoms in Ti–OH, Ti=O, C=O, and peripheral Ti=O, respectively. Figure S7, Supporting Information and Figure 3b show the survey and high-resolution XPS spectra of Ti_3C_2 QDs formed by the laser ablation for which similar conclusions about the residual presence of Al and distribution of components due to the peripheral elements (C=O at 286.5 eV, O atoms in C=O at 529.0 eV, and Ti at 457.3 eV) and C–Ti–OH groups (Ti component at 459.0 eV and O atoms at 531.3 eV) can be drawn.

While the XPS analysis of Nb_2C is analogous to those just commented for Ti_3C_2 and Ti_2C QDs, with the Nb3d and O1s peaks agreeing with the presence of C–Nb–OH and Nb=O and peripheral C=O, the analysis of these three MxQDs contrasts with that of V_2C for which the high-resolution O1s peak is far much narrower than those of the other three MxQDs in the series with a prevalent, almost-unique component at 532.3 eV that agrees well with the expected binding energy for V=O. Figures S5 and S6,

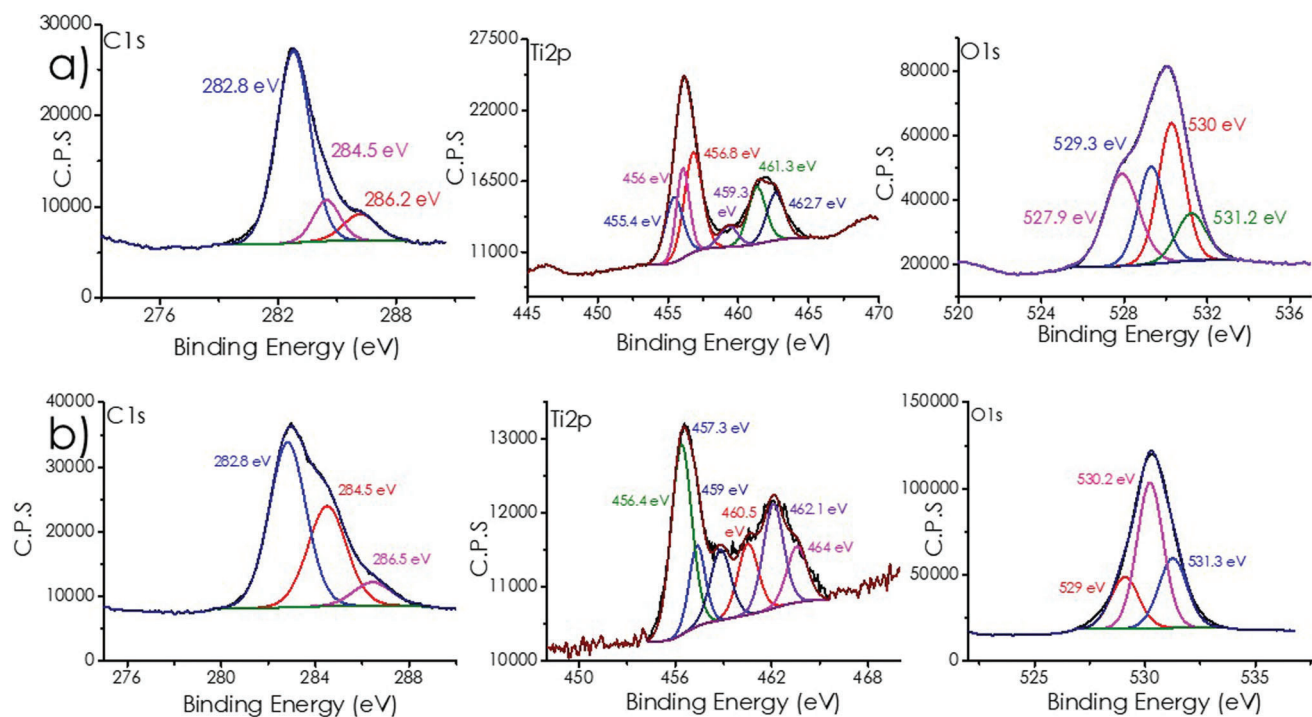


Figure 3. XPS deconvolution of the high-resolution C 1s, Ti 2p, and O 1s peaks for dry a) Ti_3C_2 and b) Ti_2C QDs formed by laser ablation.

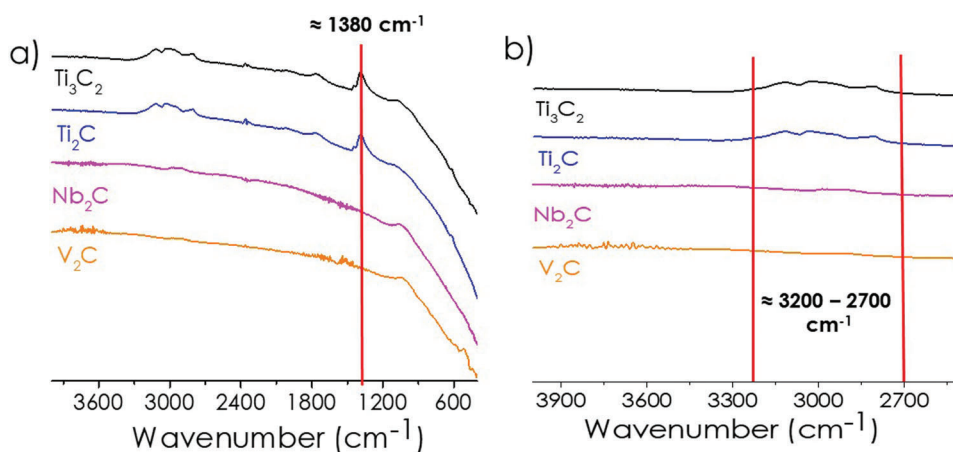


Figure 4. IR spectra of the different MXene QDs prepared in the present study marking a) the Ti-O bond vibration and b) stretching O-H region. Differences among Ti_3C_2 and Ti_2C QD samples with Nb_2C and V_2C QDs would indicate the prevalence of surface terminal OH groups in the Ti QDs and O groups in the Nb_2C and V_2C QD, respectively.

Supporting Information shows the high-resolution XPS analysis of Nb_2C and V_2C and the best deconvolution to individual components of each peak.

As commented in the introduction, MXenes can be generally obtained by the dealumination of the MAX phase in HF solutions of appropriate concentrations and conditions. This procedure results in the presence of F atoms as surface terminal groups. In the present case, however, exfoliation was performed in an aqueous suspension in the absence of any fluorinated compound. We presumed that the surface terminal groups should be oxygenated functional groups coming from the water that has also

been frequently detected by XPS even for Ti_3C_2 samples prepared in HF as defects.^[30,31] Overall XPS data provides firm support to the presence of oxygenated functional groups as terminal groups, with a prevalence for double-bonded oxygen in the case of V_2C and both hydroxyls and double-bonded O for the other three MsQDs.

To provide further experimental evidence in support of the presence of hydroxyl groups in Ti_3C_2 QDs, IR spectra of the Ti_3C_2 QD samples after the removal of H_2O and dehydration were recorded. They are presented in **Figure 4** where three stretching O-H bands in the $3200\text{--}2700\text{ cm}^{-1}$ region were recorded,

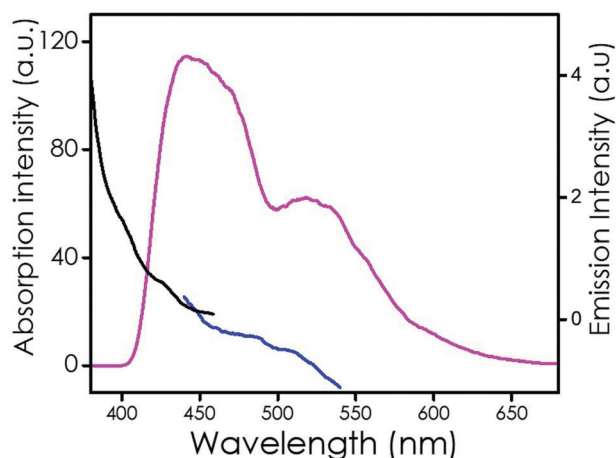


Figure 5. The emission spectrum of Ti_3C_2 MXene QDs ($\lambda_{\text{exc}} = 350$ nm, pink) and excitation spectra monitoring photoluminescence at 430 (black) and 540 (blue) nm.

indicating the presence of O-H groups in dried Ti_3C_2 QDs. The O-H stretching vibration was accompanied by peaks at about 1750, 1380, and 800 cm^{-1} . The vibration peak at 1380 cm^{-1} can be due to O-H bending,^[46] while that at 800 cm^{-1} is characteristic of the Ti-O bond vibration.^[47] These spectra lend support to the presence of -OH and O as surface terminal groups in the present case.

As commented in the introduction one of the most characteristic features of QDs, including chalcogenide QDs, carbon dots, graphene dots, and so on, is the observation of photoluminescence.^[14a,32] Photoluminescence has been already indicated as a convenient quantitative technique to follow the increase in the concentration of suspended MxQDs in the laser ablation synthesis (Figure 1b). In the case of C-dots, due to the varied distribution of trapping sites, the emission spectra are known to change as a function of the excitation wavelength.^[33] The emission has also been observed in the scarce precedents of MxQDs reported in the literature.^[16,17,21,22] While Ti_3C_2 is a conductive MXene with a small 0.1 V bandgap and it is a non-emissive material, diminution of the lateral size to the nanometric regime introduces photoluminescence for Ti_3C_2 QDs. Although the nature of the emitting species is unclear and it may derive from defects, trapping sites, and confinement, the emission is observed in semiconducting materials. In the case of Ti_3C_2 QD, it has been shown in Figure 1 that photoluminescence intensity upon 350 nm excitation increases along with the time of the laser ablation of $\text{Ti}_3\text{C}_2\text{Al}$ suspension until a stationary luminescence intensity is reached. **Figure 5** shows the emission spectrum recorded from Ti_3C_2 QDs, while Figures S1 and S2, Supporting Information show the emission and excitation spectra for Ti_3C_2 QDs and Ti_2C QDs.

In the literature, the photoluminescence of Ti_3C_2 QDs has been frequently reported as a broad emission from 400 to 700 nm, with the emission maxima shifting toward the red as the excitation wavelength increases.^[34] This excitation wavelength-dependence photoluminescence has been also observed for other QDs.^[35] In the present case, upon excitation at 350 nm, the emission spectrum of Ti_3C_2 QD exhibits two emission bands with rel-

ative λ_{em} at 430 and 540 nm. Observation of more than one emission band is uncommon and needs to be understood.^[36] The relative intensity of the two emission peaks changed along the ablation time, with the intensity of the emission peak at 430 nm increasing faster with respect to the 540 nm emission (see Figure 1). This would be compatible with the existence of different emission centers for each emission band. To support that the sites for the short (430 nm) and long (540 nm) photoluminescence are different, excitation spectra monitoring at 430 or 540 nm were recorded. The different excitation spectra confirm that the two emissions derive from different chromophores, the maximum emissions at 540 and 430 nm are reached at 350–400 nm and below 300 nm, respectively.

The photoluminescence emitted by the Ti_3C_2 QDs can be visually observed by fluorescence microscopy and this property is the base of the use of QDs in cell imaging. In accordance with the broad emission spanning from 400 to 650 nm, optical fluorescence microscopy of the Ti_3C_2 QDs with excitation at 368, 487, and 587 nm shows blue, green, and red images of these particles, respectively. **Figure 6** presents selected fluorescence images of exactly the same field, showing the spatial coincidence of this multicolor emission due to Ti_3C_2 QDs located at the circular halo of a suspension drop after solvent evaporation. Figures S8–S10, Supporting Information show an analogous comparison of white light and fluorescence images for the other three MxQDs under study.

While photoluminescence corresponding to the relaxation of an excited state indicates the semiconducting properties of Ti_3C_2 QDs, the optical absorption spectrum was used to determine the bandgap. The absorption spectrum of Ti_3C_2 QDs has been presented in Figure 1 characterized by a continuously growing absorption with an onset absorption at about 500 nm and with an absorption maximum near 400 nm. A blue shift in the absorption maximum was observed as the laser irradiation time increased, in agreement with a gradual decrease in the average lateral size of the Ti_3C_2 QDs. From the linear part of the Tauc plot of the reflectivity, the bandgap energy could be estimated as 1.94 eV.

2.2. General Applicability of the Laser Ablation Method

The previous paragraphs refer to the preparation and characterization of Ti_3C_2 QDs from the $\text{Ti}_3\text{C}_2\text{Al}$ by laser ablation in aqueous suspensions. This material was selected because it probably corresponds to the first and most researched MXene, with numerous experimental and theoretical studies reporting its properties and uses. However, the purpose of the present study was to show that the laser ablation procedure is a general method to obtain MxQDs and it can be extended to the synthesis of other MxQDs. This is an important contribution to the field since depending on the nature of the MXene, dealumination requires very different etching conditions, HF concentrations, and etching time and some MAX phases are reluctant to undergo dealumination. Aimed at the purpose of showing the general validity of the laser ablation to form MxQDs, three other MAX materials were submitted to analogous treatment as just described for the preparation of Ti_3C_2 QDs in suspension. Specifically, the other three MAX phases were Ti_2CAl , Nb_2CAl , and V_2CAl . It should be commented that at least in the case of Ti_2CAl , the exfoliation

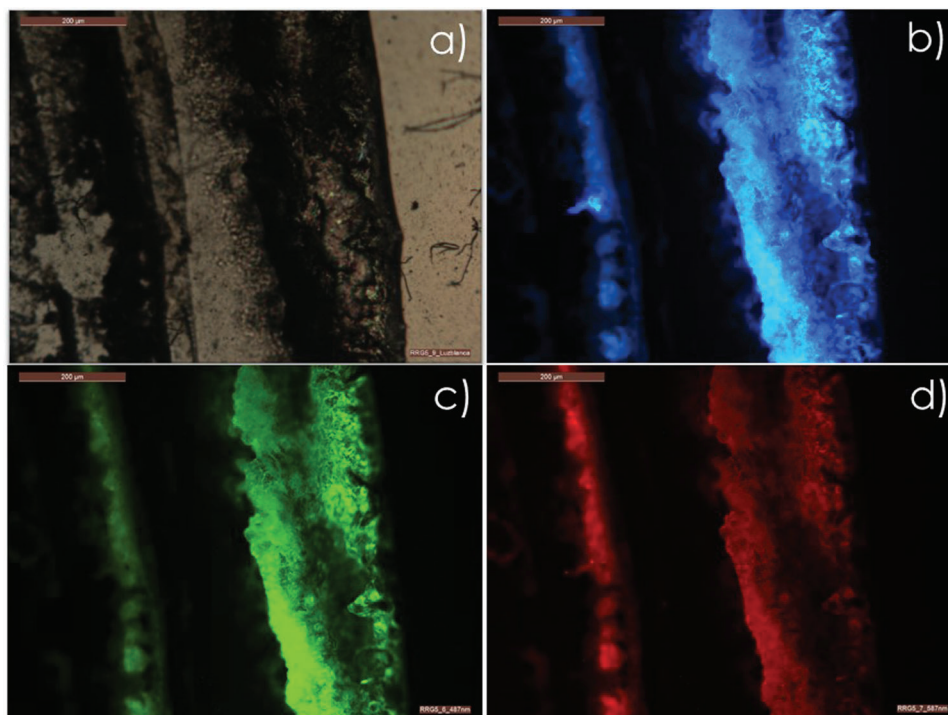


Figure 6. a) Optical and fluorescence microscopy images of Ti_3C_2 MXene QDs upon excitation at b) 368, c) 487, and d) 587 nm, respectively.

conditions have to be compatible with the lesser stability of the resulting Ti_2C . It was observed that similarly to $\text{Ti}_3\text{C}_2\text{Al}$, the three MAX phases do form the corresponding MxQD upon 532 nm pulsed laser ablation under the conditions used for $\text{Ti}_3\text{C}_2\text{Al}$ (see Figures S1–S14 in the supporting information). In all cases, the process of QD formation in the suspension could be adequately followed by UV–vis absorption spectroscopy, photoluminescence, and DLS measurements in the suspension. Supporting information provides characterization data for these other three MxQDs. As in the case of Ti_3C_2 QDs, two-step centrifugation first at 4000 rpm and then at 13 000 rpm renders MxQDs that were characterized by TEM, HR-TEM, and AFM. In every case, small QDs of average sizes between 5 and 7 nm were observed by HR-TEM with thicknesses measured by AFM of 5 nm or lower, corresponding to less than five layers of particles to monolayers. The QDs were highly crystalline and the fringes measured in the HR-TEM images corresponding to each expected MXene lattice, 0.22 for 103 of Ti_2C ,^[37] 0.23 for 006 plane of Nb_2C ,^[38] and 0.22 nm for the 103 plane of V_2C ,^[38] as reported in the literature. Particles of 1 nm height corresponding to single-layer MXene in the three cases were again frequently observed in AFM. The IR spectrum of Ti_2C QD shown in Figure 4 was almost coincident with that of Ti_3C_2 QD, showing vibration bands that are compatible with the presence of Ti–OH groups. Interestingly, although of lower overall intensity, OH groups were monitored also for Nb_2C in the 3200–2700 cm^{-1} region with a sharper band at about 1000 cm^{-1} . O–H groups were absent in the case of V_2C QD. For V_2C QD the presence of two bands at 1000 and 500 cm^{-1} was observed. In agreement with V chemistry,^[39] it is proposed that in the latter case, it should be =O groups, rather than O–H, the surface terminal groups present in the material. In the case of Nb_2C , an

intermediate situation with both O–H and =O groups could be present as surface terminal groups.^[40]

These three MxQDs exhibit also photoluminescence with two relative emissions at λ_{em} wavelengths of about 430 and 540 nm, almost coincident with those previously commented in the case of Ti_3C_2 . Variations in the relative intensity of the two emission maxima and differences in the excitation spectra for each of the two bands were observed and recorded, these features being coincident with those already commented on in detail earlier for the case of Ti_3C_2 QDs.

UV–vis absorption spectra of the MxQDs were also similar to that recorded for Ti_3C_2 QDs, with absorption onset about 500 nm increasing in intensity towards UV, although in the cases of Nb_2C QDs and V_2C QDs, the relative absorption maxima in the UV region were more clear appearing at about 260 nm. From these absorption spectra, the corresponding Tauc plots assuming an indirect semiconductor nature³ were used to estimate the corresponding bandgaps. Table 1 summarizes the four MxQDs prepared in the present study directly from the corresponding MAX phase without chemical etching agents and some data related to the average particle size and thickness, as well as bandgap energy value.

2.3. Theoretical Calculations

One of the consequences of decreasing the particle size to the nanometric dimension is the opening of a gap between occupied and unoccupied orbitals, as it can be experimentally proved by observation of photoluminescence. To gain insights into the influence of the particle size on the appearance of a band gap,

Table 1. MxQDs prepared in the present by laser ablation in suspension and some relevant characterization data..

MxQDs	Average particle size [nm] ^{a)}	Average thickness [nm] ^{b)}	Band-gap [eV]
Ti ₃ C ₂	4.0 ± 0.2	3.2	1.94
Ti ₂ C	6.2 ± 0.4	2.9	2.2
V ₂ C	3.0 ± 0.2	7.2	2.12
Nb ₂ C	7.1 ± 0.2	3.0	1.98

^{a)} Average particle sizes were obtained from the histograms of particle size distribution measured by HR-TEM. ^{b)} Estimated error 0.2 nm.

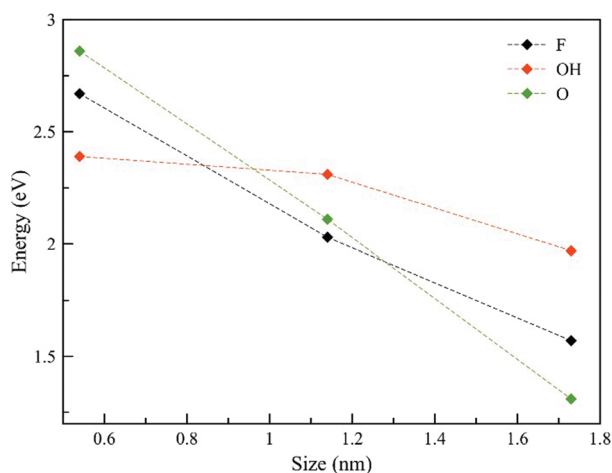


Figure 7. Computed trend of the energy gap with increasing size of the MxQDs with different terminations. Note that PBE potentials used in the present calculations underestimate the bandgap energy that should be higher than the estimated values. However, the calculation reproduces correctly the experimental trend.

theoretical calculations at the DFT level of theory on model Ti₃C QDs with increasing size and different terminations (F, OH, and O) were performed. Models based on Ti₂C were selected since they are computationally less costly due to the lesser number of atoms required, but they should provide a valid understanding also for other MxQDs. Models of three different sizes were considered, namely, 0.5, 1.1, and 1.7 nm. Larger sizes were not affordable due to the high computational cost, but the trends shown by these three models with different terminal groups should also be applicable to larger sizes.

As expected, the presence of a finite system generates the opening of an energy gap which constantly increases while decreasing the size of the MxQDs, and it strongly depends on the termination considered (Figure 7). In particular, a fast decrease in the energy gap is observed for both F and O terminations, going from 2.67 (2.86) eV for the smallest QD considered of 0.5 nm, to 1.57 (1.31) eV for systems with 1.7 nm size for the F (O) substituents. Interestingly, this bandgap energy diminution with the particle size is notably less pronounced when the OH termination is considered. In this case, the energy gap decreases from 2.4 to 2.0 eV for the same size range, suggesting higher stability of the OH-terminated MxQD. As can be seen in Figure 7, the present calculations indicate a dependence of the bandgap energy with the particle dimension, the bandgap increasing as the

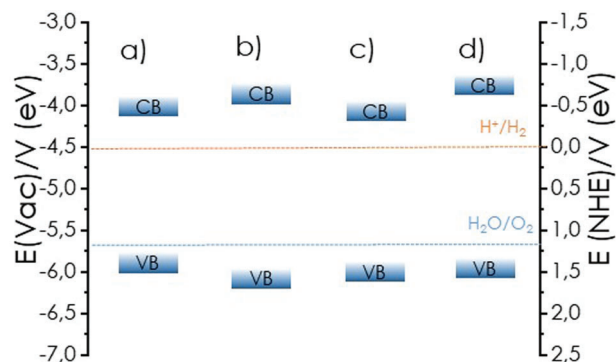


Figure 8. Energy of the valence band maximum (VB) and conduction band minimum (CB) for a) Ti₃C₂, b) Ti₂C, c) Nb₂C, and d) V₂C MxQDs.

particle size decreases and varying depending on the surface terminal groups. These results agree with previous calculations reported in the literature.^[41] Regarding the actual absolute value of the bandgap energy, it is also known that although PBE potential underestimates the bandgap energy (compare bandgap energies in Figure 7 with Table 1), these calculations provide a correct description of the bandgap energy trend as a function of structural parameters.^[42]

For the purpose of the present research, the present calculations confirm the importance of the surface terminal groups (O and OH) compared to the more common F groups as well as the importance of the particle size control. In this way, it could be possible to further control and fine-tune the bandgap of MxQDs to adjust the band energy potentials of the highest occupied and lowest unoccupied electronic states to match the desired values for a given photocatalytic reaction.

2.4. Photocatalytic Hydrogen Generation Activity

Considering the semiconducting nature of the MxQDs and the tunability of the bandgap with the particle dimension in the QD regime, these nanoparticles are good candidates as photocatalysts for hydrogen evolution reactions. To establish the thermodynamic feasibility of the process, we initially determine experimentally the redox potential of the valence and conduction band of the MxQDs to know how they are aligned with the oxidation and reduction potential of water. The valence band for each material was calculated by extrapolating the linear fitting of the first peak appearing in the XPS spectrum to zero intensity corrected by the work function of the instrument (see Figures S11–S14, Supporting Information). Starting with this value, the conduction band was estimated by adding the value of the band gap previously calculated from the Tauc plot (Figures S11–S14, Supporting Information). Figure 8 presents a diagram of the valence and conduction band energy values of the MxQDs where it is observed that the potentials of the corresponding MxQDs are well aligned to promote hydrogen and oxygen evolution reactions from water. Ti₃C₂ and Nb₂C MXQDs are the MxQDs with the best-aligned conduction and valence band potentials (Figure 8), coinciding with those that give the best response in the photocatalytic reaction, as can be seen later.

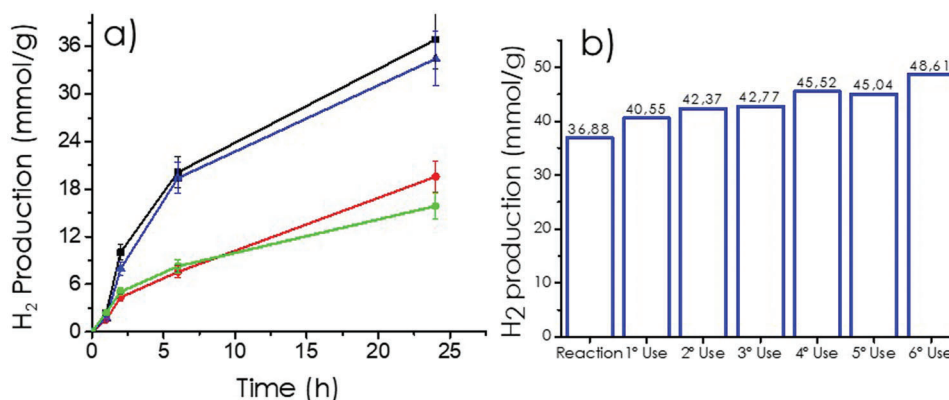


Figure 9. a) H₂ evolution reaction curve for ■ Ti₃C₂; ▼ Nb₂C; ● Ti₂C; and ◇ V₂C; and b) reuses of Ti₃C₂ MxQDs.

Then, the photocatalytic activity for H₂ generation was evaluated for the corresponding MxQDs, in the presence of triethanolamine (TEOA) as a sacrificial electron donor with visible light ($\lambda > 450$ nm) by filtering the output of a 300 W Xe lamp. Suspensions (20 mL) of the four MxQDs at the same 0.2 optical density at 300 nm were irradiated through quartz in a photoreactor (51 mL) in an H₂O:TEOA 4:1 mixture. H₂ evolution was observed for the four MxQD samples. The reactions were carried out in quadruplicate with differences lesser than 10% among them. The temporal H₂ evolution is presented in **Figure 9**. These temporal profiles show that the rate of H₂ evolution decreases over time, a fact that is commonly observed and can be attributed to the depletion of the sacrificial agent, formation of by-products from the sacrificial agent acting as poisons, and the reverse reaction of H₂ formation with photogenerated holes oxidizing H₂ to H⁺.^[48] As can be seen there, the H₂ production at 24 h irradiation follows the order V₂C < Ti₂C < Nb₂C < Ti₃C₂. It was interesting to note that the performance of Ti₃C₂ and Nb₂C QDs as H₂ evolution photocatalysts is similar, rendering values that are among the highest ever reported for H₂ evolution reaction using visible light. Table S1, Supporting Information provides a comparison with the literature. As can be seen there, the photocatalytic activity of Ti₃C₂ QDs (2.02 mmol g⁻¹ h⁻¹) is among the best-performing material with a H₂ production rate similar to that of Pt/g-C₃N₄ (2.5 mmol g⁻¹ h⁻¹) and Pt/C-dots@UiO-66(Zr)-NH₂-g-C₃N₄ (2.95 mmol g⁻¹ h⁻¹), but these photocatalysts contain Pt as co-catalyst, while Ti₃C₂ QDs is noble metal free. Regarding the much higher photocatalytic performance indicated in Table S1, Supporting Information for CdS, it should be remarked the lack of stability of this sulfide due to photocorrosion and the presence of a toxic transition metal. Worth commenting on is the only precedent in which Y2CF2 Mxene was used as a semiconductor, finding that it was not stable in water in 10 h runs and producing H₂ in acetonitrile and TEOA at an initial rate of 9 $\mu\text{mol} \times \text{g}^{-1} \times \text{h}^{-1}$ using Pt as co-catalyst. In the present case, the MxQDs were stable exhibiting much higher photocatalytic activity and without Pt as a co-catalyst.^[49]

The stability of Ti₃C₂ QDs as a photocatalyst was tested by a series of seven consecutive uses. An apparent gradual increase in the photocatalytic activity of the material was observed reaching a final H₂ productivity at 24 h of 48.6 mmols_{H₂} \times g⁻¹. To further assess the stability of Ti₃C₂ QDs the seven-times used ma-

terial was characterized by TEM and AFM (Figures S15 and S16, Supporting Information). No differences between the used and fresh samples in terms of particle morphology, size distribution, or crystallinity were observed by TEM. However, both TEM and AFM, indicate an apparent agglomeration of the MxQDs with an increase in thickness. It could be that the stress during the photocatalytic reactions, with continued charge separation, leads to a re-stacking of the nanometric thick QDs and their aggregation as a consequence of the particle charge. However, this agglomeration does not influence the photocatalytic hydrogen evolution.

To provide some support to the generation of a photoinduced charge separation state upon QD irradiation, methyl viologen (MV²⁺) was used as a visual probe of photoinduced electron transfer. Upon single electron reduction, MV²⁺ gives rise to the corresponding MV^{•+} radical cation that in the absence of oxygen behaves as a long-lived species in the aqueous phase. MV^{•+} can be characterized conventional optical absorption spectroscopy by its characteristic UV-vis absorption spectrum responsible for the visual blue/green color developed in solution. A blank control irradiation MV²⁺ in the same conditions, but in the absence of Ti₃C₂ QDs did not result in the observation of MV^{•+}. In contrast, when an aqueous suspension of Ti₃C₂ QDs containing 10⁻³ M of MVCl₂ and a few drops of methanol as an electron donor was irradiated, the solution become increasingly blue and the UV-vis spectrum of the resulting suspension shown in **Figure 10** indicates the formation of MV^{•+} radical cation. Generation of MV^{•+} upon irradiation is a strong experimental evidence of the photoinduced electron transfer from Ti₃C₂ QD in its excited state to MV²⁺ resulting in the generation of MV^{•+} and a positive electron hole on the Ti₃C₂ QD. This positive electron hole on Ti₃C₂ QD will be quenched by methanol as an electron donor.

3. Conclusion

While most of the general procedures for MXene synthesis require HF or strong Lewis acids, there is a need to develop alternative green procedures. Herein, we have reported that 532 nm laser ablation in liquid suspension in the absence of any aggressive reagent produces MXene QDs. It has been shown that the method of laser ablation in aqueous suspension is quite general for the formation of MxQDs from the MAX phases. Other solvents can equally be employed. The process of MxQD formation

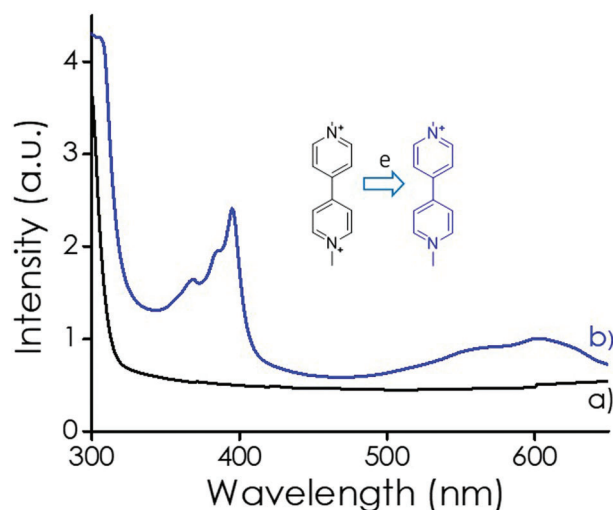


Figure 10. UV-vis spectrum of Ti_3C_2 suspension in the presence of MV^{2+} as an electron acceptor in H_2O with a few methanol drops: a) before and b) after xenon lamp irradiation.

can be conveniently followed by the increase in the optical absorption in the UV and photoluminescence intensity as well as by dynamic laser scattering of the suspension. HR-TEM imaging confirms the crystallinity of the materials and their MXene structure with an average lateral particle size of 5 nm, while according to their thickness measured by AFM, most of them are constituted by a single layer or few layers of MXene QDs. Importantly, the procedure leads to oxygen-terminated MXenes, IR spectroscopy suggesting the presence in some cases of terminal O-H (Ti_3C_2 and Ti_2C QD) and O (V_2C QD) groups. The trend in the bandgap energy as a function of the particle size and surface termination of these MxQDs has been estimated by DFT calculations that in general shows how powerful and simple is the control of the bandgap in MXenes if the synthesis of samples is sufficiently precise to provide samples with narrow particle size distribution, appropriate size, and surface terminal groups. This strategy should lead to effective band engineering.^[43] The bandgap opening in QDs has allowed us to determine the photocatalytic H_2 generation activity in the absence of photosensitizing dyes, giving values in the order of $\text{mmol}_{\text{H}_2} \times \text{g}^{-1}$ that are in the range of the best photocatalysts, even without further optimization. The present study has opened the way to bandgap engineering of MXenes by controlling their lateral size in the dimensions of a few nanometers and adequate surface functionalization. The MxQDs can be easily obtained using laser ablation with beams of adequate beam spot area and power.

4. Experimental Section

All MAX phases used as precursors (Ti_3AlC_2 , Ti_2AlC , Nb_2AlC , and V_2AlC) in the laser ablation in the liquid phase were supplied by Nanochemazone and used without further purification.

Material Preparation: The preparation of MxQDs was carried out by suspending the MAX phase (3 mg) in water (4 mL). The suspension was sonicated in order to obtain a persistent dispersion, transferred in a 10×10 mm, 4 mL quartz cuvette capped with a septum, and bubbled through a needle for 15 min with argon before photolysis. The dispersion was irra-

diated with the second harmonic of a Q-switched Nd:YAG laser (Quantel Brilliant, 532 nm, 50 mJ pulse⁻¹, 5 ns fwhm, frequency 1 Hz). Laser power was measured with a power meter, placing the probe head at the sample holder. Formation of MxQD from the MAX phase, due to the mechanical shock induced by the laser hit on the particle was followed by measuring periodically the optical absorption and photoluminescence ($\lambda_{\text{ex}} = 350$ nm) of the cuvette, directly. Alternatively, the particle size evolution of MXenes in suspension and stability of the suspension was determined from a 0.2 mL aliquot that was analyzed by dynamic laser scattering and zeta potential. Ablation measurements were performed for 2 h. After this time the MxQDs present in suspension were separated from other particles by sedimentation of large particles by centrifugation in two stages, first at 4000 rpm for 4 h and, subsequently, 13 000 rpm for 1 h. MxQDs remained in the supernatant after discarding the sediments in the two centrifugation steps. The solid MxQD material was obtained by freeze-drying removal of the solvent.

Photocatalytic Experiments: The photocatalytic reactions were carried out using a suspension of the corresponding MxQDs obtained after the two-stage centrifugation with the corresponding mass that was redispersed in 16 mL of Milli-Q water adding 4 mL of triethanolamine (TEOA) as a sacrificial electron donor. The mass of MxQDs was 1 mg. Before starting the irradiation, the aqueous suspension containing TEOA and the photocatalyst was purged with Ar for at least 15 min to remove air from the photoreactor. The suspension was stirred at room temperature and irradiated with a 300 W Xenon lamp equipped with a cut-off filter ($\lambda > 450$ nm) to ensure irradiation with visible light. Throughout the experiment, the temperature of the system was monitored and the pressure was analyzed by the manometer adapted to the photoreactor. The evolving gases were analyzed from the head space connecting directly the photoreactor to an Agilent 490 Micro GC system (Molsieve 5 Å column using Ar as carrier gas) without manual handling. Hydrogen gas evolution was quantified using a calibration plot obtained by injecting into the micro-GC two mixtures of known H_2 concentration. The reactions were carried out four times for each sample with differences lower than 10% in the values of H_2 evolution. Reuses were carried out for Ti_3C_2 QDs using the same amounts, volumes, solvents, and conditions as above. After 24 h, the lamp was switched off and the system was exhaustively purged with Ar to remove the gases in the reactor headspace until GC analysis did not detect H_2 . At that moment, the system was irradiated again without the removal of the Ti_3C_2 QDs and the course of the reaction was periodically analyzed by GC. The same procedure was repeated in each reuse.

Generation of MV^+ was performed by adding 0.4 mL of an aqueous 1 M MVCl_2 solution to 3.6 mL of Ti_3C_2 QDs suspension in a quartz cuvette. A few methanol drops were added. The cuvette was capped with a septum, purged with Ar using needles, and irradiated with visible light from a filtered (> 450 nm) Xe lamp beam. The solution becomes quickly blue and the optical absorption spectrum periodically recorded coincides with that reported for MV^+ radical cation.^[44]

Characterization: Optical absorption spectra were recorded on the same cuvette in which the laser ablation treatment was performed using a Cary 100 UV-vis-NIR spectrophotometer in the transmission mode.

Photoluminescence spectra were recorded in an Edinburgh FLS900 instrument. The sample was placed in an appropriate 1×1 cm² quartz cuvette capped with a septum. The samples were purged with Ar prior to recording the photoluminescence. For the measurement of the MxQD evolution upon laser ablation, the same cuvette exposed to the 532 nm laser pulsed was placed in the spectrophotometer without any treatment, using 350 nm as excitation wavelength. Excitation spectra were recorded monitoring either at 430 or 540 nm for MxQDs suspensions that were submitted to the two-step centrifugation process in a fluorescence quartz cuvette capped with rubber septum after Ar purging for 15 min.

X-ray photoelectron spectra (XPS) of MxQDs were collected with a SPECS spectrometer equipped with an MCD-9 detector using a monochromatic Al ($K_{\alpha} = 1486.6$ eV) X-ray source operating under an ultrahigh vacuum at 1.3×10^{-13} atm. The binding energies were corrected for surface charge effects during measurements using the central level of C 1s (284.5 eV) as the internal reference. CASA software has been employed for spectra deconvolution.

ICP-OES analysis was used to determine the metal content of MxQDs after dissolving them in concentrated aqua regia.

ATR-FTIR spectra of MxQDs were measured with a Bruker Tensor 27 instrument. Prior to ATR-FTIR measurements, the solid samples were heated in an oven at 100 °C overnight to remove physisorbed water.

The morphology and composition of MxQDs were characterized using a SEM instrument (Zeiss instrument, AURIGA Compact) coupled with an EDX detector. High-resolution TEM images were acquired on a JEOL JEM 2100F under an accelerating voltage of 200 kV. Prior to recording the image, the suspension was sonicated and a microdrop was cast onto a carbon-coated copper TEM holder and the solvent was allowed to evaporate before inserting into the microscope chamber.

Atomic force microscopy (AFM) was used to determine the thickness of the samples obtained by laser ablation. In this case, the measurements were carried out on the tap mode with a Multimode Nanoscope 3A instrument that has a vertical subnanometric resolution and a horizontal resolution of about 5 nm.

Computational Details: To ensure the presence of quantum dots, the initial structures were inserted in a periodic cell in which all the dimensions were increased to assure the presence of vacuum along the three directions, in between 1–2.5 nm, to avoid the presence of spurious interactions with image cells. Due to the fast increase in computational cost with the increase of the size of the MxQD, only dimensions below 2 nm were considered (i.e., Ti₂C-OH with 1.7 nm size consists of 200 atoms).

The geometry optimization of the different MxQDs was performed using the PBE ultrasoft pseudopotential with the Quantum Espresso 6.5 software.^[45–47] A plane wave basis set was used with an energy cutoff of 45, 60, and 50 Ry for the F, OH, and O terminated structures and a charge cutoff of 360, 480, and 400 Ry, respectively. The geometry optimization criteria were set to 10^{−5} eV for energy and to 0.001 eV Å^{−1} for forces on each atom. The calculations were performed at the gamma K-point, and an orbital mixing of 0.4 was applied for the whole calculation. All calculations were spin-polarized, with initial magnetization on Ti atoms. After the optimized geometries were obtained, a single point calculation was performed with the Gaussian16 software, with the CAM-B3LYP functional and the 6-3G(d) basis set for light elements, while for Ti the Lanl2dz pseudopotential was used.^[48]

Supporting Information

Supporting Information is available from the Wiley Online Library or from the author.

Acknowledgements

Financial support by the Spanish Ministry of Science and Innovation (Severo Ochoa CEX2021-001230S and PDI2021-126971-CO2-OB-1 both funded by the MCIN/AEI/10.13039/501100011033) and Generalitat Valenciana (Prometeo 2021-038) is gratefully acknowledged. R.R.G. and A.M. also thank, respectively, the Spanish Ministry of Science and Innovation and the Generalitat Valenciana for postgraduate scholarships. S.O. thanks the “Excellence Initiative – Research University” (IDUB) Program, Action I.3.3 – “Establishment of the Institute for Advanced Studies (IAS)” for funding (grant no. UW/IDUB/2020/25) and the Polish National Agency for Academic Exchange under the Bekker program (grant no. PPN/BEK/2020/1/00053/U/00001). This research was carried out with the support of the Interdisciplinary Center for Mathematical and Computational Modeling at the University of Warsaw (ICM UW) under grant nos. G83-28 and GB80-24.

Conflict of Interest

The authors declare no conflict of interest.

Data Availability Statement

The data that support the findings of this study are available from the corresponding author upon reasonable request.

Keywords

MAX phase laser ablation, MXene photocatalysts, MXene quantum dots, photocatalytic hydrogen evolution

Received: January 16, 2023
Published online: February 25, 2023

- [1] A. VahidMohammadi, J. Rosen, Y. Gogotsi, *Science* **2021**, *372*, eabf1581.
- [2] M. Naguib, M. W. Barsoum, Y. Gogotsi, *Adv. Mater.* **2021**, *33*, 2103393.
- [3] M. Naguib, V. N. Mochalin, M. W. Barsoum, Y. Gogotsi, *Adv. Mater.* **2014**, *26*, 992.
- [4] X. Li, C. Wang, Y. Cao, G. Wang, *Chem. – Asian J.* **2018**, *13*, 2742.
- [5] K. R. G. Lim, M. Shekhirev, B. C. Wyatt, B. Anasori, Y. Gogotsi, Z. W. Seh, *Nat. Synth.* **2022**, *1*, 601.
- [6] J. A. Kumar, P. Prakash, T. Krithiga, D. J. Amarnath, J. Premkumar, N. Rajamohan, Y. Vasseghian, P. Saravanan, M. Rajasimman, *Chemosphere* **2022**, *286*, 131607.
- [7] X. Zhan, C. Si, J. Zhou, Z. Sun, *Nanoscale Horiz.* **2020**, *5*, 235.
- [8] J.-C. Lei, X. Zhang, Z. Zhou, *Front. Phys.* **2015**, *10*, 276.
- [9] J. Halim, I. Persson, E. J. Moon, P. Kühne, V. Darakchieva, P. O. Å. Persson, P. Eklund, J. Rosen, M. W. Barsoum, *J. Phys.: Condens. Matter* **2019**, *31*, 165301.
- [10] K. Huang, C. Li, H. Li, G. Ren, L. Wang, W. Wang, X. Meng, *ACS Appl. Nano Mater.* **2020**, *3*, 9581.
- [11] R. Tang, S. Xiong, D. Gong, Y. Deng, Y. Wang, L. Su, C. Ding, L. Yang, C. Liao, *ACS Appl. Mater. Interfaces* **2020**, *12*, 56663.
- [12] J. Zhang, N. Kong, S. Uzun, A. Levitt, S. Seyedin, P. A. Lynch, S. Qin, M. Han, W. Yang, J. Liu, *Adv. Mater.* **2020**, *32*, 2001093.
- [13] K. Hantanasirisakul, M. Alhabeab, A. Lipatov, K. Maleski, B. Anasori, P. Salles, C. Ieosakulrat, P. Pakawatpanurut, A. Sinitskii, S. J. May, *Chem. Mater.* **2019**, *31*, 2941.
- [14] K. Hantanasirisakul, M. Q. Zhao, P. Urbankowski, J. Halim, B. Anasori, S. Kota, C. E. Ren, M. W. Barsoum, Y. Gogotsi, *Adv. Electron. Mater.* **2016**, *2*, 1600050.
- [15] H. Kim, H. N. Alshareef, *ACS Mater. Lett.* **2019**, *2*, 55.
- [16] Z. Liu, H. N. Alshareef, *Adv. Electron. Mater.* **2021**, *7*, 2100295.
- [17] B. Anasori, C. Shi, E. J. Moon, Y. Xie, C. A. Voigt, P. R. Kent, S. J. May, S. J. Billinge, M. W. Barsoum, Y. Gogotsi, *Nanoscale Horiz.* **2016**, *1*, 227.
- [18] M. M. Sajid, S. B. Khan, Y. Javed, N. Amin, Z. Zhang, N. A. Shad, H. Zhai, *Environ. Sci. Pollut. Res.* **2021**, *28*, 35911.
- [19] L. Zhang, W. Su, H. Shu, T. Lü, L. Fu, K. Song, X. Huang, J. Yu, C.-T. Lin, Y. Tang, *Ceram. Int.* **2019**, *45*, 11468.
- [20] Y. Zhang, X.-H. Zha, K. Luo, N. Qiu, Y. Zhou, J. He, Z. Chai, Z. Huang, Q. Huang, Y. Liang, *J. Phys. Chem. C* **2019**, *123*, 6802.
- [21] C. E. Shuck, K. Ventura-Martinez, A. Goad, S. Uzun, M. Shekhirev, Y. Gogotsi, *ACS Chem. Health Saf.* **2021**, *28*, 326.
- [22] M. Bacon, S. J. Bradley, T. Nann, *Part. Part. Syst. Character.* **2014**, *31*, 415.
- [23] L. P. Kouwenhoven, D. Austing, S. Tarucha, *Rep. Prog. Phys.* **2001**, *64*, 701.
- [24] S. Y. Lim, W. Shen, Z. Gao, *Chem. Soc. Rev.* **2015**, *44*, 362.
- [25] G. Bhuvanewari, S. Radjarejiesri, *Int. J. ChemTech Res.* **2015**, *8*, 104.

- [26] K. Grieve, P. Mulvaney, F. Grieser, *Curr. Opin. Colloid Interface Sci.* **2000**, *5*, 168.
- [27] A. J. Sutherland, *Curr. Opin. Solid State Mater. Sci.* **2002**, *6*, 365.
- [28] P. Khanna, N. Singh, *Faguang Xuebao* **2007**, *127*, 474.
- [29] J. I. Kim, J. Kim, J. Lee, D.-R. Jung, H. Kim, H. Choi, S. Lee, S. Byun, S. Kang, B. Park, *Nanoscale Res. Lett.* **2012**, *7*, 482.
- [30] C. Xia, S. Zhu, T. Feng, M. Yang, B. Yang, *Adv. Sci.* **2019**, *6*, 1901316.
- [31] P. Atienzar, A. Primo, C. Lavorato, R. Molinari, H. Garcia, *Langmuir* **2013**, *29*, 6141.
- [32] X. T. Zheng, A. Ananthanarayanan, K. Q. Luo, P. Chen, *Small* **2015**, *11*, 1620.
- [33] S. Zhu, Y. Song, X. Zhao, J. Shao, J. Zhang, B. Yang, *Nano Res.* **2015**, *8*, 355.
- [34] H. G. Baldovi, M. Latorre-Sánchez, I. Esteve-Adell, A. Khan, A. M. Asiri, S. A. Kosa, H. Garcia, *J. Nanopart. Res.* **2016**, *18*, 240.
- [35] Q. Xue, H. Zhang, M. Zhu, Z. Pei, H. Li, Z. Wang, Y. Huang, Y. Huang, Q. Deng, J. Zhou, *Adv. Mater.* **2017**, *29*, 1604847.
- [36] A. S. Sharbirin, S. Akhtar, J. Kim, *Opto-Electron. Adv.* **2021**, *4*, 200077.
- [37] X. Yu, X. Cai, H. Cui, S.-W. Lee, X.-F. Yu, B. Liu, *Nanoscale* **2017**, *9*, 17859.
- [38] M. Safaei, M. R. Shishehbore, *J. Mater. Sci.* **2021**, *56*, 17942.
- [39] S. Iravani, R. S. Varma, *Nanomaterials* **2022**, *12*, 1200.
- [40] A. Rafeerad, W. Yan, G. L. Sequiera, N. Sareen, E. Abu-El-Rub, M. Moudgil, S. Dhingra, *Adv. Healthcare Mater.* **2019**, *8*, 1900569.
- [41] J. Shao, J. Zhang, C. Jiang, J. Lin, P. Huang, *Chem. Eng. J.* **2020**, *400*, 126009.
- [42] Y. Yuan, L. Jiang, X. Li, P. Zuo, X. Zhang, Y. Lian, Y. Ma, M. Liang, Y. Zhao, L. Qu, *Adv. Mater.* **2022**, *34*, 2110013.
- [43] Y. Xuan, R.-Y. Zhang, X.-S. Zhang, J. An, K. Cheng, C. Li, X.-L. Hou, Y.-D. Zhao, *Nanotechnology* **2018**, *29*, 355101.
- [44] R. Wang, X. Wang, Y. Sun, *Sens. Actuators, B* **2017**, *241*, 73.
- [45] H. Zeng, X. W. Du, S. C. Singh, S. A. Kulinich, S. Yang, J. He, W. Cai, *Adv. Funct. Mater.* **2012**, *22*, 1333.
- [46] J. M. Thompson, *Infrared Spectroscopy*, Jenny Stanford Publishing, New York **2018**.
- [47] S. Sakka, F. Miyaji, K. Fukumi, *J. Non-Cryst. Solids* **1989**, *112*, 64.
- [48] S. Navalón, A. Dhakshinamoorthy, M. Álvaro, B. Ferrer, H. García, *Chem. Rev.* **2023**, *123*, 445.
- [49] K. Maeda, H. Wakayama, Y. Washio, A. Ishikawa, M. Okazaki, H. Nakata, S. Matsuishi, *J. Phys. Chem. C* **2020**, *124*, 14640.